nanomaterials

MDPI

Article

Highly Sensitive Photothermal Fiber Sensor Based on MXene Device and Vernier Effect

Qing Wu [1,†], Si Chen [2,†], Lixin Guan [2] and Haibin Wu [1,*]

[1] Heilongjiang Province Key Laboratory of Laser Spectroscopy Technology and Application, Harbin University of Science and Technology, Harbin 150080, China; wuqing@hrbust.edu.cn
[2] School of Physics and Electronic Information, Gannan Normal University, Ganzhou 341000, China; chensics9@163.com (S.C.); lxguan@gnnu.edu.cn (L.G.)
* Correspondence: woo@hrbust.edu.cn
† These authors contributed equally to this work.

Abstract: A photothermal fiber sensor based on a microfiber knot resonator (*MKR*) and the Vernier effect is proposed and demonstrated. An *MXene* $Ti_3C_2T_x$ nanosheet was deposited onto the ring of an *MKR* using an optical deposition method to prepare photothermal devices. An *MXene MKR* and a bare *MKR* were used as the sensing part and reference part, respectively, of a Vernier-cascade system. The optical and photothermal properties of the bare *MKR* and the *MXene MKR* were tested. $Ti_3C_2T_x$ was applied to a photothermal fiber sensor for the first time. The experimental results showed that the modulation efficiency of the *MXene MKR* was 0.02 nm/mW, and based on the Vernier effect, the modulation efficiency of the cascade system was 0.15 nm/mW. The sensitivity was amplified 7.5 times. Our all-fiber photothermal sensor has many advantages such as low cost, small size, and good system compatibility. Our sensor has broad application prospects in many fields. The proposed stable *MKR* device based on two-dimensional-material modification provides a new solution for improving the sensitivity of optical fiber sensors.

Keywords: tapered fiber; two-dimensional material; fiber optic sensor; Vernier effect

Citation: Wu, Q.; Chen, S.; Guan, L.; Wu, H. Highly Sensitive Photothermal Fiber Sensor Based on MXene Device and Vernier Effect. *Nanomaterials* **2022**, *12*, 766. https://doi.org/10.3390/nano12050766

Academic Editors: Francesc Viñes Solana and Weichun Huang

Received: 5 January 2022
Accepted: 22 February 2022
Published: 24 February 2022

1. Introduction

Fiber optic sensors have the advantages of a large dynamic range, high sensitivity, good system compatibility, and a compact structure, and they are an attractive technology that has a wide range of application prospects in the fields of detection, medical diagnosis, and environmental monitoring [1]. The basic structure of a fiber optic sensing system includes a light source, an incident fiber, a modulation region, an exit fiber, and a detector. A fiber optic sensing element modulates an optical signal (intensity, frequency, wavelength, phase, polarization, etc.) according to changes in the modulation zone. The structures commonly used in phase fiber sensors include interferometer and resonator structures. Optical fiber sensors with the interferometer structure often use a tapered-fiber-based sensing device. Tapered fiber has the advantages of low loss, a high evanescent field, and easy integration, and is a breakthrough in the fabrication of miniaturized photonic devices, including phase fiber sensors [2]. Tapered-fiber-based photonic device microfiber knot resonators (*MKRs*, tapered fiber knotting) are one of the research hotspots in the field of phase fiber sensors. *MKRs* have the advantages of strong anti-interference, a fast response speed, high resolution, a small size, and stable measurement; thus, they have attracted much attention in the field of fiber optic sensors [3,4].

Due to the development of science and technology, the sensitivity of sensors is increasing. As an effective method to improve sensitivity, the Vernier effect has been widely used to improve the accuracy and sensitivity of measuring instruments, such as barometers, temperature sensors, humidity sensors, refractive index sensors, and so on [5,6]. The Vernier

effect in the field of fiber optic sensors is usually in the form of cascading and parallel interference structures. Fiber optic interferometers include the Mach–Zehnder interferometer (MZI), the Michelson interferometer (MI), the Fabry–Perot interferometer (FPI), and the Sagnac interferometer (SI). It is well-known that waveguides, highly nonlinear fibers, fiber gratings, and the in-line MZI have the disadvantages of high cost and poor compatibility and tunability when applied to sensors. MZIs have large losses and mode interference, which cause spectrum confusion. MZI and MI structures are extremely sensitive to disturbances from ambient temperature and stress, resulting in poor environmental stability [7]. *MKR*-based devices have high reliability, which facilitates stability of the system; low loss and high coupling efficiencies, which facilitate compatibility with fiber optic systems; and a small volume, which facilitates driving production and system integration. These devices are suitable for a Vernier-cascade system and have been widely discussed [8].

Two-dimensional, nanomaterial-modified *MKRs* provide new ideas for fiber optic sensors [9,10]. Two-dimensional materials have been gradually explored in academic research concerning their practical applications [11–14]. *MXenes*, a rapidly developing two-dimensional material family, have been reported in many studies since the first successful preparation of *MXene* $Ti_3C_2T_x$ in 2011 [15]. In 2015, *MXene* was first applied in the field of optics, and in 2017, it was applied in the field of sensors [16]. Many experimental and theoretical studies revealed the great application potential of the *MXenes* family in the fields of optoelectronics, photonics, catalysis, and energy [17–19]. The photothermal conversion efficiency of *MXene* $Ti_3C_2T_x$ is ~100%, and the thermal conductivity coefficient of *MXene* $Ti_3C_2T_x$ is 56 $WM^{-1}K^{-1}$, which expands its application to photothermal-related fields such as thermal management and photothermal fiber sensors [20,21].

We present a highly sensitive photothermal fiber sensor based on an MXene-$Ti_3C_2T_x$-deposited *MKR* and bare *MKR* cascade. *MXene* $Ti_3C_2T_x$ was fabricated using an aqueous acid etching method and deposited onto the ring of an *MKR* utilizing an optical deposition method. The spectral response of the *MXene*-deposited *MKR* was investigated, showing good resonant properties and a good photothermal response. When a control light (a 980 nm pump that the laboratory can provide) was shone onto the ring of the *MXene MKR* through a collimator, the *MXene* $Ti_3C_2T_x$ absorbed the light and generated heat. A large amount of heat changed the refractive index of the device, thereby changing the phase of the signal light. The *MXene MKR* was the sensing part of the cascade system and the bare *MKR* was the reference part. The photothermal modulation efficiency of the sensing part was 0.02 nm/mW and that of the cascade system was 0.15 nm/mW. The corresponding sensitivity was amplified 7.5 times. Our proposed integrated device, *MXene-MKR*, is small in size and suitable for packaging in compact single-unit systems, highlighting its potential for providing a new method for high-sensitivity optical sensing applications.

2. Material Characterization and Device Fabrication

2.1. Material Characterization

MXene $Ti_3C_2T_x$ was prepared via an aqueous acid etching method [22,23]. At room temperature, 40 mL of 40 wt % HF aqueous solution was mixed with Ti_3AlC_2 MAX powder (1 g) and stirred for 20 h. After using corrosion technology, we rinsed the precipitate in the mixed solution with deionized water to ensure that the pH value of the solution was greater than 6. Then, the $Ti_3C_2T_x$ solution was centrifuged at 18,000 rpm for 30 min. The supernatant was removed to retain the precipitate, and the precipitate was dried in a vacuum drying oven for later use. A simple and gentle exfoliation named the freeze-and-thaw method was used to prepare $Ti_3C_2T_x$ nanosheets [24]. We added 40 mg as-prepared *MXene* power to 40 mL deionized water and stirred the dispersion for 10 min. Afterwards, the dispersion was placed in a refrigerator at 4 °C for cooling; then, it was placed in a refrigerator at −20 °C for several hours. We took out the frozen dispersion and thawed it naturally at room temperature. Then, the *MXene* suspension was treated with an ultrasonic water bath for 1 h. This freeze-and-thaw process was repeated several times to improve the yield of $Ti_3C_2T_x$ nanosheets. Finally, the suspension was centrifuged at 3000 rpm for 30 min;

then, it was centrifuged at a speed of 18,000 rpm for 30 min. Final nanosheets from the $Ti_3C_2T_x$ dispersion were obtained by eliminating the additional solution and redispersing the sediment in water.

Characterization methods were used to study the MAX phase material, and it was successfully exfoliated into *MXene* nanosheets. Transmission electron microscopy (TEM), selected area electron diffraction (SAED), and energy dispersive spectrometer (EDS) images were employed to investigate the characterization of the delaminated $Ti_3C_2T_x$ nanosheets. The morphology of the delaminated nanosheets was studied by TEM. The morphology of the final product was investigated using TEM, and the result is presented in Figure 1a, showing that it was a nanosheet structure with lateral dimensions of 450–714 nm. Moreover, the crystal structure of the nanosheets was further studied by SAED. The results are shown in Figure 1b, indicating that the hexagonal-structure nanosheets had high crystallinity [25–27]. EDS was used to investigate the elemental distribution of *MXene* nanosheets. STEM was used to record the morphology of an investigated nanosheet; then, EDS was used to measure the elemental distribution of the nanosheet. The elemental mapping (Figure 1d–f) shows that Ti, C, and F elements are evenly distributed throughout the nanosheet range in Figure 1c, indicating that the $Ti_3C_2T_x$ nanosheets were successfully prepared. The F element belonged to the termination group of *MXene* and was caused by the HF etching process.

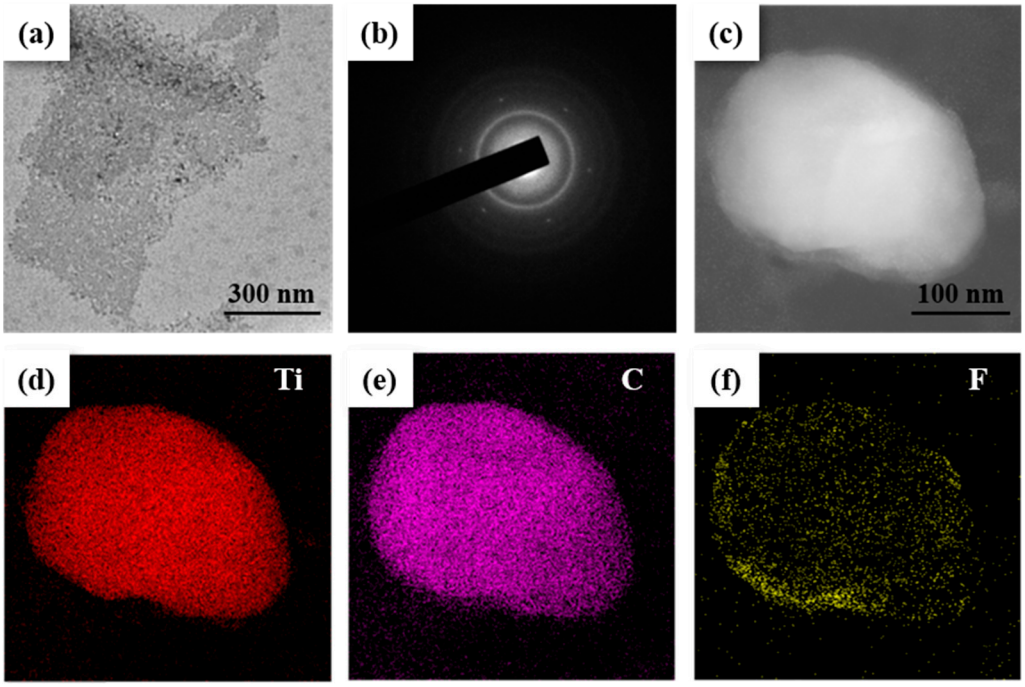

Figure 1. Characterization of *MXene* $Ti_3C_2T_x$: (**a**) TEM image of the $Ti_3C_2T_x$ nanoflakes; (**b**) SAED patterns of the $Ti_3C_2T_x$ nanoflakes; (**c**) STEM of a $Ti_3C_2T_x$ nanoflake; (**d**–**f**) elemental maps of the nanoflake in Figure (**c**), which were obtained from the EDS results.

A Raman spectrum (Figure 2a) of $Ti_3C_2T_x$ was used to further study the structure of the nanosheets. For $Ti_3C_2T_x$, characteristic peaks at 154.8, 264.3, 425, and 609.3 cm^{-1} have been previously observed [28,29]. Regarding our nanosheets, a characteristic peak at 157 cm^{-1} belonged to TiO_2, which was possibly caused by oxidation of the $Ti_3C_2T_x$ surface during the preparation process. The Raman spectrum further illustrated that *MXene* nanosheets were successfully fabricated. Furthermore, the linear absorption property of $Ti_3C_2T_x$ was investigated, and the result is presented in Figure 2b. The absorption spectrum demonstrates the ultrabroad absorption properties of the nanosheets ranging from 250 to 2000 nm, which indicates that this *MXene* material can operate under a wide range of wavelengths. This was attributed to the narrow band gap of $Ti_3C_2T_x$ [30].

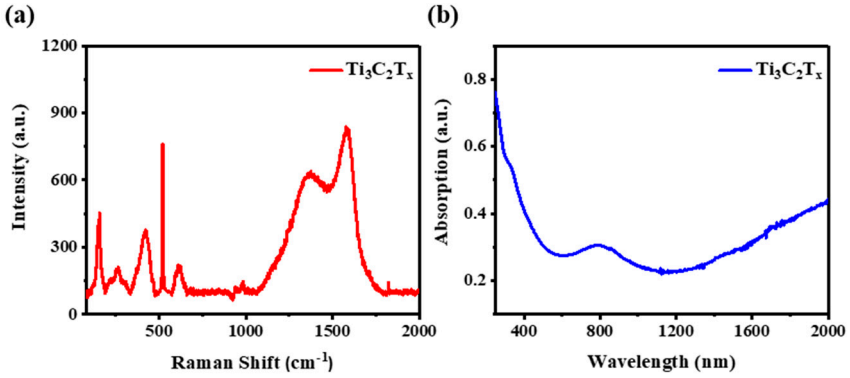

Figure 2. (**a**) the Raman spectrum of $Ti_3C_2T_x$; (**b**) UV–Vis–NIR absorption spectrum.

2.2. Devices

MXene-deposited tapered fiber is an important component in the proposed photothermal fiber sensor. Tapered fiber with waist length of 1–2 cm and waist diameter of 1–3 μm was prepared using the oxyhydrogen flame method. Tapered fiber has a long and thin waist with a good toughness that is conducive to knotting. *MKR* was prepared by knotting the tapered fiber. Two *MKR*s were prepared, and their spectral responses were tested using a broadband amplified spontaneous emission (ASE OS8143 China) source as shown in Figure 3a. This illustration corresponds to a microscope picture of the *MKRs*, where *MKR*_1 and *MKR*_2 had diameters of 900 and 1050 μm, respectively, and the corresponding tapered fiber diameter was 3μm. The *MXene-MKR* was prepared by coupling between the near-field surface of tapered fiber and *MXene* $Ti_3C_2T_x$. An optical deposition system is shown in Figure 3a. The output power of the ASE source was set at 40 mW, and a *MXene* dispersion liquid dropped to the vicinity of the *MKR* and slowly spread to the *MKR* ring. Due to the strong evanescent field of the tapered fiber, the material was adsorbed to the surface of the tapered fiber. In the process of material deposition, the deposition length of material and the loss of device were recorded in real time, and the deposition parameters were controlled by the power of the light source and the amount of material. Optical microscope images of the *MXene* before and after deposition are shown in Figure 3b. The photothermal effect of the *MXene-MKR* was measured utilizing infrared thermal imaging (FLIR E60 USA) of the control light (980 nm pump light). The control light was irradiated onto the ring of the *MKR* using infrared thermal imaging (FLIR E60), which measured the photothermal effect of the device. As shown in Figure 3c, the temperatures of the bare *MKR* and *MXene-MKR* were 23.1 and 35.3 °C, respectively, at a pump power of 200 mW. This shows that *MXene* played a key role in raising the temperature. The transmission spectra of the *MKR*s are shown in Figure 3d–f. The free spectral ranges (*FSRs*) corresponding to *MKR*_1 and *MKR*_2 were 0.585 and 0.505 nm, respectively, according to the formula $FSR = \lambda^2/(\pi D \cdot n_{eff})$, where λ is an incident wavelength, D is the diameter of the *MKR*, and n_{eff} is an effective refractive index [31]. The calculated *FSRs* of *MKR*_1 and *MKR*_2 were 0.586 and 0.502 nm, respectively, which is consistent with our experimental results. As *MKR*_2 had a larger diameter and was more conducive to deposition materials, we chose *MKR*_2 as the sensing device and *MKR*_1 as the reference device. Figure 3f is a transmission spectrum of *MXene*-deposited *MKR*_2. The transmission spectrum shows that the loss of the device increased and the resonant wavelength shifted before and after deposition.

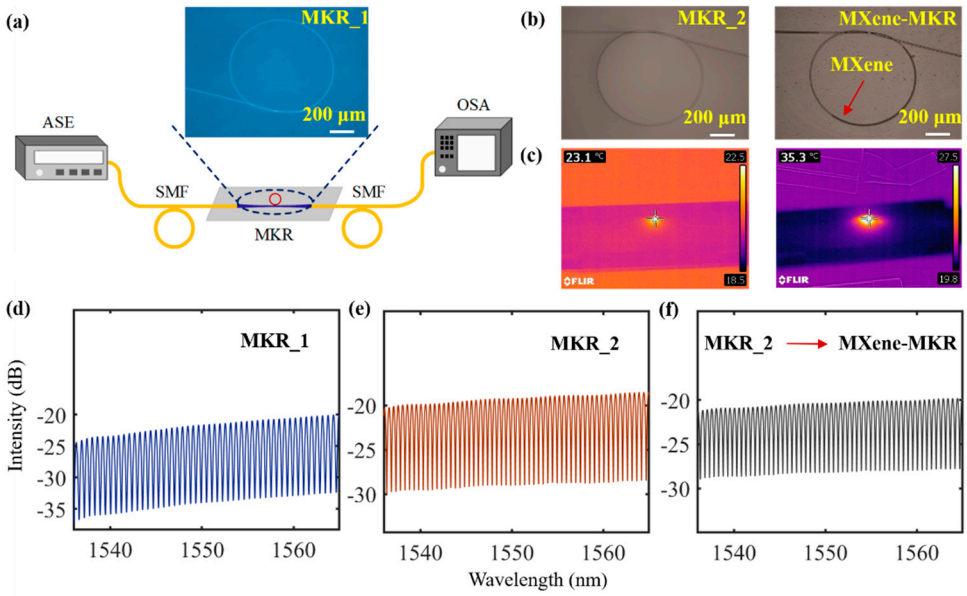

Figure 3. (**a**) Diagram of system apparatus for testing spectral response; (**b**) optical microscope image; (**c**) thermograms of bare *MKR* and *MXene MKR*; transmission spectra of (**d**) *MKR*_1, (**e**) *MKR*_2, and the (**f**) *MXene MKR*.

3. Experimental Setup and Results

3.1. Experimental Setup

The configuration of our photothermal fiber sensor is shown in Figure 4, where *MKR*_1 is the reference part, the *MXene-MKR* is the sensing part, and the *FSRs* of the *MKRs* are FSR_{MKR} and $FSR_{MXene\text{-}MKR}$. The signal light was 1550 nm, generated by an ASE light source, and the control light was 980 nm, generated by a pump light source (can be provided). The output of the system was connected to an optical spectrum analyzer (OSA, Yokogawa AQ6370D, Japan). The control light irradiated *MXene* $Ti_3C_2T_x$ onto the ring of the *MXene-MKR* through a collimator, and the *MXene* $Ti_3C_2T_x$ absorbed the pump light. The photothermal effect of *MXene* $Ti_3C_2T_x$ is a large amount of heat production, and the thermo-optical effect is a change in the refractive index of the sensor, thereby changing the phase of the signal light. The corresponding transmission spectrum is moved. The introduction of the optical Vernier effect can greatly improve sensor sensitivity, and the sensor sensitization effect can be realized by amplifying the *FSR* value of the sensing part. Vernier calipers are widely used in high-precision and short-distance ranging. The Vernier effect refers to a large change in the range of alignment indexing caused by small measurement changes. There are some similar physical parameters in the form of scale in optics. For example, the transmission spectrum of a broad-spectrum light source through an *MKR* is a comb spectrum. The peak spacing of the two *MKRs* produces a minimal difference, and the two devices can be cascaded to create an optical Vernier effect. A small shift in the spectrum of one device magnifies the spectral shift of the cascade system several times, which improves measurement sensitivity while maintaining a larger measurement range. When the resonator *MXene-MKR* structure is modulated by an external sensor signal, the *MXene MKR* and *MKR*_1 cascade and the Vernier interference fringes drift. The amount of stripe movement is far more than the drift of the spectral fringes of the *MXene-MKR*, which is the basis for realizing high-modulation-efficiency sensing.

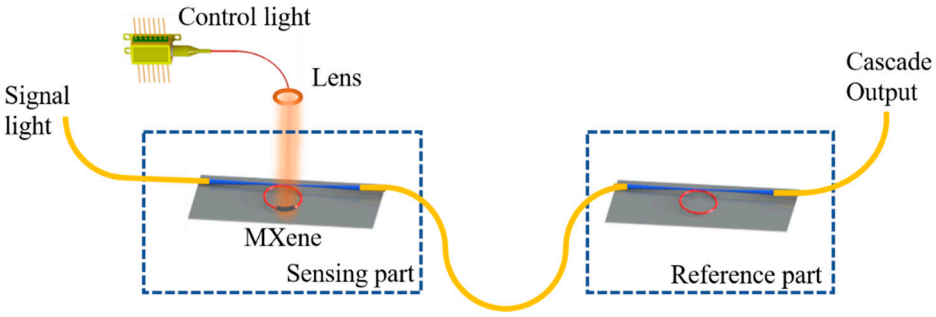

Figure 4. Experimental setup of photothermal fiber sensor based on *MKR* and *MXene-MKR* cascade.

Based on the Vernier effect [32], the *FSR* of the envelope can be defined as:

$$FSR_{envelope} = \frac{FSR_{MKR} \cdot FSR_{MXene-MKR}}{|FSR_{MKR} - FSR_{MXene-MKR}|} = \frac{\lambda^2}{\pi \cdot n_{eff} |D_{MKR} - D_{MXene-MKR}|} \quad (1)$$

Compared to the phase shift of *MKR*_1, the phase shift of the cascade sensor is amplified by K_s times, and the value of K_s is:

$$K_s = \frac{FSR_{MKR}}{|FSR_{MKR} - FSR_{MXene-MKR}|} = \frac{D_{MXene-MKR}}{|D_{MKR} - D_{MXene-MKR}|} \quad (2)$$

The spectrum of the cascaded sensor is composed of a fine-comb spectrum and a large envelope. Firstly, at least one complete envelope period must be observed within the limited wavelength range of the light source. Secondly, the cascaded superposition spectrum must be regular and periodic, that is, both FSR_{MKR} and $FSR_{MXene\text{-}MKR}$ must be regular and periodic. A cascade system based on the Vernier effect needs to satisfy the condition that the sensor is sensitive to variables while the reference part is insensitive to variables. According to the above analysis, the closer the D_{MKR} and $D_{MXene\text{-}MKR}$ values, the higher the sensing modulation efficiency.

3.2. Experimental Results

In the cascade system, the transmission spectra of the reference part and the sensing part are shown in Figure 5a,b, respectively, and the corresponding *FSRs* were 0.585 and 0.505 nm, respectively. The transmission spectrum of the cascade system is shown in Figure 5c, and the *FSR* was 3.73 nm. A pump light generated by a laser diode was directly illuminated by a cylindrical lens pointed toward the ring of the *MKR* with *MXene* $Ti_3C_2T_x$. Due to a photothermal effect, the material absorbed the 980 nm pump light, producing a large amount of heat and changing the refractive index of the device. The transmission spectrum of *MXene-MKR* achieved a phase shift when a pump light was applied to a material-based device. When the pump power was 34 mW, the transmission spectrum moved 0.505 nm in the long wavelength direction, and the corresponding cascading system moved 3.8 nm (as shown in Figure 6).

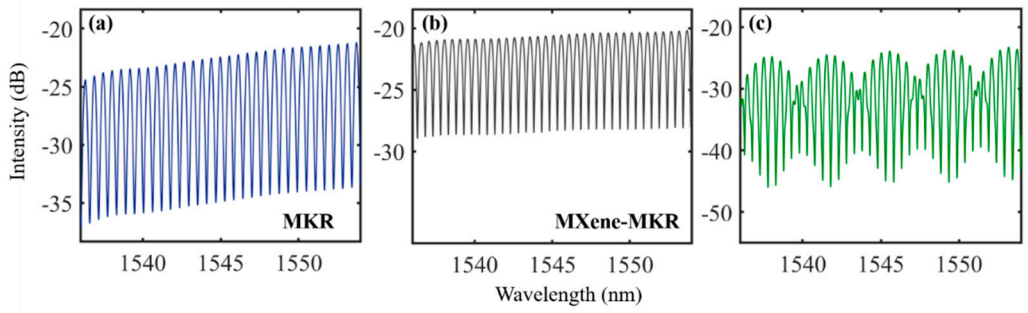

Figure 5. Transmission spectra of the (**a**) *MKR*; (**b**) *MXene-MKR*; (**c**) cascade system.

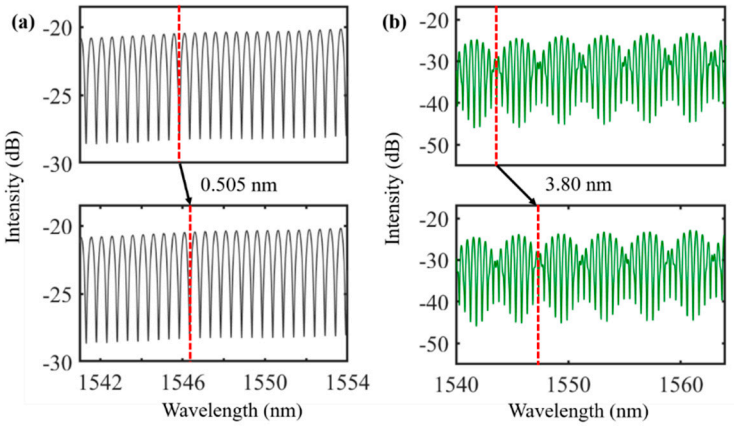

Figure 6. Wavelength shift of (**a**) *MXene-MKR* and (**b**) the cascade system at a pump power of 34 mW.

When the pump power was increased from 0 to 250 mW (which was the maximum power), *MXene-MKR*'s transmission spectrum (without the Vernier effect) moved 4.8 nm, and the corresponding modulation efficiency was 0.02 nm/mW. For a cascading system of the entire Vernier, when the optical intensity was increased from 0 to 250 mW, the long wavelength direction moved 38 nm, the modulation efficiency of the cascade system was 0.15 nm/mW (as shown in Figure 7), and the calculated *K* of the system was 7.5, which is in line with the theoretical value (K_s = 7.49).

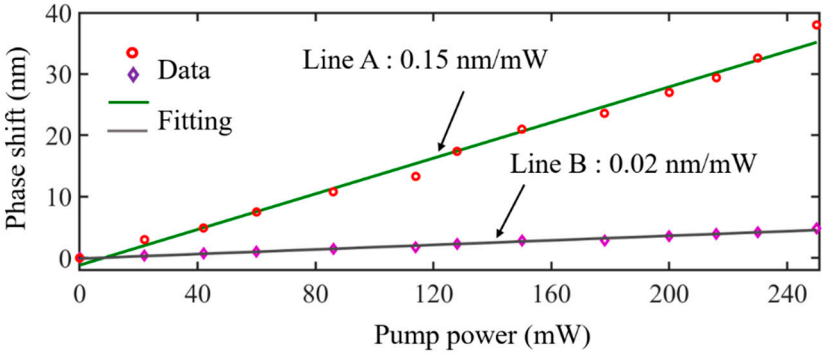

Figure 7. Modulation efficiency of (Line A) *MXene-MKR* and (Line B) cascade system.

4. Discussion

In this work, an all-fiber cascade *MKR* and *MKR-MXene* photothermal sensor were constructed. This sensor has advantages including small size, low power consumption, and good compatibility, and it is economical as well. This study is the first time that *MXene* $Ti_3C_2T_x$ with a high photothermal conversion efficiency has been applied to the field of photothermal sensors. Our selection of photothermal materials takes into account the advantages of *MXene* $Ti_3C_2T_x$, such as high thermal conductivity, a high photoinduced damage threshold, greater flexibility, good electrical conductivity, good tunability of the electronic band structure, good broadband saturation absorption, and so on, and is conducive to the preparation of photothermal devices. The photothermal conversion efficiency of *MXene* $Ti_3C_2T_x$ is ~100%, which is beyond the reach of other two-dimensional materials. In the context of structure and devices, the damage threshold of *MXene* $Ti_3C_2T_x$ loaded on tapered fiber is high, and the device is stable. Both the structure coupling and interference mechanism of *MKR*s are wavelength-sensitive, which is beneficial to their application in the sensing field.

Compared to MZI- and MI-type tapered fiber optic sensors, the *MKR* structure adopted by our system has better stability performance. It also has a simpler structure and is easier to make as an integrated sensor. The MZI and the MI have the problems of wavelength drift and environmental instability, and such systems have too many devices, which leads

to a large footprint and is not conducive to integration. For the sensitivity of our system, the diameter of the *MKR* can be adjusted to obtain greater sensitivity. The taper fiber prepared for the *MKR* has a smaller diameter, and the sensitivity of *MXene* $Ti_3C_2T_x$ per unit length is greater than that of photothermal fiber sensors with interferometer structures.

Due to the limitations of experimental conditions, only a 980 nm pump light was used to control the light. The absorption spectrum of *MXene* $Ti_3C_2T_x$ is 250–2000 nm, which can realize photothermal sensing in different bands. The family of *MXenes* aids the development and exploration of new materials and allows us to obtain required materials through functional group regulation, providing a new idea for optical sensors based on two-dimensional materials. As *MKR*s can be used in formats such as parallel, series, and other ways, later works may prepare a multipoint, high-sensitivity, multiparameter sensor system. As a functional, two-dimensional material, *MXenes* provide an economical and practical platform for creating high-efficiency fiber sensors with antielectromagnetic interference and good compatibility.

5. Conclusions

In summary, *MXene* $Ti_3C_2T_x$ was successfully prepared using a HF acid etching method. The wide spectrum absorption of *MXene* $Ti_3C_2T_x$ shows its potential to be used in the fabrication of photonic devices. We demonstrated a sensitivity-enhanced cascade photothermal fiber sensor based on *MXene* $Ti_3C_2T_x$. *MKR-MXene* was the sensor device, the control light was a 980 nm pump light, and the corresponding modulation efficiency was 0.02 nm/mW. A bare *MKR* was used as the reference part. After the system cascaded, the modulation efficiency was 0.15 nm/mW, and the sensitivity was increased 7.5 times, which is consistent with the theoretical value. The preparation process of *MXene* $Ti_3C_2T_x$ is relatively mature, and this material has a high photothermal conversion efficiency, a wide spectrum detection range, and a large population. *MXene* $Ti_3C_2T_x$ has great application potential in optoelectronic devices. Our proposed device based on an *MKR* using *MXene* $Ti_3C_2T_x$ has a small footprint, is suitable for packaging and integration, and highlights a new idea for high-performance optical sensing applications.

Author Contributions: Conceptualization, Q.W., S.C., L.G. and H.W.; methodology, Q.W.; software, Q.W. and S.C.; investigation, Q.W., S.C. and H.W.; resources, L.G. and H.W.; data curation, L.G. and H.W.; writing—original draft preparation, Q.W. and S.C.; writing—review and editing, Q.W., S.C., L.G. and H.W.; supervision, L.G. and H.W. All authors have read and agreed to the published version of the manuscript.

Funding: This work was supported by the National Natural Science Foundation of China (Nos. 42061067).

Data Availability Statement: Not applicable.

Conflicts of Interest: The authors declare no conflict of interest.

References

1. Talataisong, W.; Ismaeel, R.; Brambilla, G. A Review of Microfiber-Based Temperature Sensors. *Sensors* **2018**, *18*, 461. [CrossRef] [PubMed]
2. Ali, N.; Azzuhri, S.R.; Johari, M.A.M.; Rashid, H.; Khudus, M.I.M.A.; Razak, M.Z.A.; Chen, Z.; Misran, N.; Arsad, N. Effects of Tungsten Disulphide Coating on Tapered Microfiber for Relative Humidity Sensing Applications. *Sensors* **2021**, *21*, 7132. [CrossRef] [PubMed]
3. Luo, W.; Chen, Y.; Xu, F. Recent Progress in Microfiber-Optic Sensors. *Photonic Sens.* **2021**, *11*, 45–68. [CrossRef]
4. Dang, H.; Chen, M.; Li, J. A Highly-Sensitive Temperature-Sensor Based on a Microfiber Knot-Resonator Packaged in Polydimethylsiloxane. *IEEE Photonics J.* **2021**, *13*, 1–8. [CrossRef]
5. Martens, D.; Bienstman, P. Comparison between Vernier-cascade and MZI as transducer for biosensing with on-chip spectral filter. *Nanophotonics* **2017**, *6*, 703–712. [CrossRef]
6. Shao, L.-Y.; Luo, Y.; Zhang, Z.; Zou, X.; Luo, B.; Pan, W.; Yan, L. Sensitivity-enhanced temperature sensor with cascaded fiber optic Sagnac interferometers based on Vernier-effect. *Opt. Commun.* **2015**, *336*, 73–76. [CrossRef]
7. Wang, R.; Wu, Q.; Jiang, X.; Fan, T.; Guo, J.; Wang, C.; Zhang, F.; Gao, Y.; Zhang, M.; Luo, Z.; et al. A few-layer InSe-based sensitivity-enhanced photothermal fiber sensor. *J. Mater. Chem. C* **2020**, *8*, 132–138. [CrossRef]

8. Liu, Y.; Li, X.; Zhang, Y.-N.; Zhao, Y. Fiber-optic sensors based on Vernier effect. *Measurement* **2021**, *167*, 108451. [CrossRef]
9. Zhang, L.; Tang, Y.; Tong, L. Micro-/Nanofiber Optics: Merging Photonics and Material Science on Nanoscale for Advanced Sensing Technology. *iScience* **2020**, *23*, 100810. [CrossRef]
10. Huang, W.; Ma, C.; Li, C.; Zhang, Y.; Hu, L.; Chen, T.; Tang, Y.; Ju, J.; Zhang, H. Highly stable *MXene* (V_2CT_x)-based harmonic pulse generation. *Nanophotonics* **2020**, *9*, 2577–2585. [CrossRef]
11. Girei, S.H.; Alkhabet, M.M.; Kamil, Y.M.; Lim, H.N.; Mahdi, M.A.; Yaacob, M.H. Wavelength Dependent Graphene Oxide-Based Optical Microfiber Sensor for Ammonia Gas. *Sensors* **2021**, *21*, 556. [CrossRef]
12. Wang, M.; Zhu, J.; Zi, Y.; Wu, Z.-G.; Hu, H.; Xie, Z.; Zhang, Y.; Hu, L.; Huang, W. Functional two-dimensional black phosphorus nanostructures towards next-generation devices. *J. Mater. Chem. A* **2021**, *9*, 12433–12473. [CrossRef]
13. Huang, W.; Zhu, J.; Wang, M.; Hu, L.; Tang, Y.; Shu, Y.; Xie, Z.; Zhang, H. Emerging Mono-Elemental Bismuth Nanostructures: Controlled Synthesis and Their Versatile Applications. *Adv. Funct. Mater.* **2021**, *31*, 2007584. [CrossRef]
14. Huang, W.; Wang, M.; Hu, L.; Wang, C.; Xie, Z.; Zhang, H. Recent Advances in Semiconducting Monoelemental Selenium Nanostructures for Device Applications. *Adv. Funct. Mater.* **2020**, *30*, 2003301. [CrossRef]
15. Naguib, M.; Kurtoglu, M.; Presser, V.; Lu, J.; Niu, J.; Heon, M.; Hultman, L.; Gogotsi, Y.; Barsoum, M.W. Two-Dimensional Nanocrystals Produced by Exfoliation of Ti_3AlC_2. *Adv. Mater.* **2011**, *23*, 4248–4253. [CrossRef] [PubMed]
16. Gogotsi, Y.; Anasori, B. The Rise of MXenes. *ACS Nano* **2019**, *13*, 8491–8494. [CrossRef] [PubMed]
17. Wu, Q.; Jin, X.; Chen, S.; Jiang, X.; Hu, Y.; Jiang, Q.; Wu, L.; Li, J.; Zheng, Z.; Zhang, M.; et al. MXene-based saturable absorber for femtosecond mode-locked fiber lasers. *Opt. Express* **2019**, *27*, 10159–10170. [CrossRef] [PubMed]
18. Wu, Q.; Chen, S.; Wang, Y.Z.; Wu, L.M.; Jiang, X.T.; Zhang, F.; Jin, X.X.; Jiang, Q.Y.; Zheng, Z.; Li, J.Q.; et al. MZI-Based All-Optical Modulator Using *MXene* Ti_3C2T_x (T = F, O, or OH) Deposited Microfiber. *Adv. Mater. Technol.* **2019**, *4*, 10. [CrossRef]
19. Huang, W.; Hu, L.; Tang, Y.; Xie, Z.; Zhang, H. Recent Advances in Functional 2D MXene-Based Nanostructures for Next-Generation Devices. *Adv. Funct. Mater.* **2020**, *30*, 2005223. [CrossRef]
20. Li, R.; Zhang, L.; Shi, L.; Wang, P. MXene Ti_3C_2: An Effective 2D Light-to-Heat Conversion Material. *ACS Nano* **2017**, *11*, 3752–3759. [CrossRef]
21. Huang, W.; Zhang, Y.; You, Q.; Huang, P.; Wang, Y.; Huang, Z.N.; Ge, Y.; Wu, L.; Dong, Z.; Dai, X.; et al. Enhanced Photodetection Properties of Tellurium@Selenium Roll-to-Roll Nanotube Heterojunctions. *Small* **2019**, *15*, e1900902. [CrossRef] [PubMed]
22. Jiang, X.T.; Liu, S.X.; Liang, W.Y.; Luo, S.J.; He, Z.L.; Ge, Y.Q.; Wang, H.D.; Cao, R.; Zhang, F.; Wen, Q.; et al. Broadband Nonlinear Photonics in Few-Layer *MXene* $Ti_3C_2T_x$ (T = F, O, or OH). *Laser Photonics Rev.* **2018**, *12*, 10. [CrossRef]
23. Anasori, B.; Lukatskaya, M.R.; Gogotsi, Y. 2D metal carbides and nitrides (MXenes) for energy storage. *Nat. Rev. Mater.* **2017**, *2*, 17. [CrossRef]
24. Huang, X.W.; Wu, P.Y. A Facile, High-Yield, and Freeze-and-Thaw-Assisted Approach to Fabricate *MXene* with Plentiful Wrinkles and Its Application in On-Chip Micro-Supercapacitors. *Adv. Funct. Mater.* **2020**, *30*, 1910048. [CrossRef]
25. Shi, C.; Beidaghi, M.; Naguib, M.; Mashtalir, O.; Gogotsi, Y.; Billinge, S.J.L. Structure of Nanocrystalline Ti_3C_2 *MXene* Using Atomic Pair Distribution Function. *Phys. Rev. Lett.* **2014**, *112*, 125501. [CrossRef]
26. Iqbal, M.; Fatheema, J.; Noor, Q.; Rani, M.; Mumtaz, M.; Zheng, R.K.; Khan, S.A.; Rizwan, S. Co-existence of magnetic phases in two-dimensional MXene. *Mater. Today Chem.* **2020**, *16*, 100271. [CrossRef]
27. Li, Z.Y.; Wang, L.B.; Sun, D.D.; Zhang, Y.D.; Liu, B.Z.; Hu, Q.K.; Zhou, A.G. Synthesis and thermal stability of two-dimensional carbide *MXene* Ti_3C_2. *Mater. Sci. Eng. B-Adv. Funct. Solid-State Mater.* **2015**, *191*, 33–40. [CrossRef]
28. Hu, T.; Wang, J.; Zhang, H.; Li, Z.; Hu, M.; Wang, X. Vibrational properties of Ti_3C_2 and $Ti_3C_2T_2$ (T = O, F, OH) monosheets by first-principles calculations: A comparative study. *Phys. Chem. Chem. Phys.* **2015**, *17*, 9997–10003. [CrossRef]
29. Chen, L.; Huang, K.; Xie, Q.; Lam, S.M.; Sin, J.C.; Su, T.; Ji, H.; Qin, Z. The enhancement of photocatalytic CO_2 reduction by the in situ growth of TiO_2 on Ti_3C_2 MXene. *Catal. Sci. Technol.* **2021**, *11*, 1602–1614. [CrossRef]
30. Zhang, X.; Zhang, Z.H.; Zhou, Z. MXene-based materials for electrochemical energy storage. *J. Energy Chem.* **2018**, *27*, 73–85. [CrossRef]
31. Wu, Q.; Huang, W.; Wang, Y.; Wang, C.; Zheng, Z.; Chen, H.; Zhang, M.; Zhang, H. All-Optical Control of Microfiber Knot Resonator Based on 2D Ti_2CT_x MXene. *Adv. Opt. Mater.* **2020**, *8*, 1900977. [CrossRef]
32. Troia, B.; De Leonardis, F.; Passaro, V.M.N. Cascaded ring resonator and Mach-Zehnder interferometer with a Sagnac loop for Vernier-effect refractive index sensing. *Sens. Actuators B Chem.* **2017**, *240*, 76–89. [CrossRef]